

# Respiratory Self-Navigation for Whole-Heart Bright-Blood Coronary MRI: Methods for Robust Isolation and Automatic Segmentation of the Blood Pool

Davide Piccini,<sup>1\*</sup> Arne Littmann,<sup>2</sup> Sonia Nielles-Vallespin,<sup>3</sup> and Michael O. Zenge<sup>2</sup>

**Free-breathing three-dimensional whole-heart coronary MRI is a noninvasive alternative to X-ray coronary angiography. However, the existing navigator-gated approaches do not meet the requirements of clinical practice, as they perform with suboptimal accuracy and require prolonged acquisition times. Self-navigated techniques, applied to bright-blood imaging sequences, promise to detect the position of the blood pool directly in the readouts acquired for imaging. Hence, the respiratory displacement of the heart can be calculated and used for motion correction with high accuracy and 100% scan efficiency. However, additional bright signal from the chest wall, spine, arms, and liver can render the isolation of the blood pool impossible. In this work, an innovative method based on a targeted combination of the output signals of an anterior phased-array surface coil is implemented to efficiently suppress such additional bright signal. Furthermore, an algorithm for the automatic segmentation of the blood pool is proposed. Robust self-navigation is achieved by cross-correlation. These improvements were integrated into a three-dimensional radial whole-heart coronary MRI sequence and were compared with navigator-gated imaging in vivo. Self-navigation was successful in all cases and the acquisition time was reduced up to 63%. Equivalent or slightly superior image quality, vessel length, and sharpness were achieved. Magn Reson Med 68:571–579, 2012.**

© 2011 Wiley Periodicals, Inc.

**Key words:** coronary MRI; self-navigation; respiratory motion compensation; three-dimensional radial; phased-array coil; free-breathing

Whole-heart MR angiography represents an appealing non-invasive alternative to X-ray coronary angiography, which eliminates the dangerous exposure to ionizing radiation (1,2). In addition, free-breathing, whole-heart MR imaging is clinically relevant for the assessment of congenital heart diseases and for the planning of electrophysiology procedures. To avoid artifacts due to the periodic contraction of the heart, the coronary MRI acquisition is electrocardiogram (ECG-) triggered and image data are acquired, over a large number of heartbeats, in end diastole, when there

is minimal myocardial motion (3). Henceforth, a group of readouts acquired within a single heartbeat will be referred to as an interleave. A common approach to compensate for respiratory motion consists of the use of a beam navigator (4). Such navigator is usually placed on the dome of the right hemidiaphragm and provides feedback on the respiratory position of the diaphragm (5) along the major direction of respiratory motion, namely the superior–inferior (SI) direction. A gating window is defined in end expiration, such that only the interleaves acquired within the window are used for the final reconstruction. All the other interleaves are discarded and reacquired. Prospective motion compensation, known as tracking, can be additionally performed on interleaves acquired within the gating window by means of a fixed correlation factor (6). Although major improvements in navigator-gated coronary MRI have been achieved in recent years (7–9), there is still a number of outstanding problems that limited the clinical usage of this technique. 1) Respiratory gating performs with an acceptance rate of less than 40%, in many cases. 2) An ill-positioned navigator (10), as well as irregularities on the respiratory pattern of the patient (11) might lead to extended examination times. In cases where the variation in respiratory motion is very large, adaptive windowing techniques (7,9) are not reliable and the acquisition might not be completed. 3) The accuracy of the motion detection performed with the navigator is suboptimal, as the fixed correlation factor does not take the interpatient variability into account (6), and is adversely affected by hysteretic effects (12) and temporal delays (13).

Respiratory self-navigation has recently been introduced to overcome these drawbacks (14,15). The goal of this method is to assess the information on the respiratory motion directly from the one-dimensional (1D) fast Fourier transform (FFT) of readouts acquired at the beginning of each interleave and which can be interpreted as projections of the imaging volume onto the SI axis. The SI projection of each interleave is compared with a reference projection acquired at the beginning of the examination to determine the respiratory offset. This enables to perform motion correction directly in *k*-space during image reconstruction with: 1) an acceptance rate of 100%, 2) simplified examination planning and an a priori knowledge of the duration of the acquisition regardless of the individual respiratory patterns, and 3) improved accuracy of the motion compensation. Radial three-dimensional (3D) trajectories are particularly well suited for this application, as they combine straightforward adaptation to self-navigation (14,16) with intrinsic robustness against motion (17) and low sensitivity to radial undersampling (18,19). However,

<sup>1</sup>Pattern Recognition Lab, Department of Computer Science, Friedrich-Alexander University of Erlangen-Nuremberg, Erlangen, Germany

<sup>2</sup>MR Applications and Workflow Development, Healthcare Sector, Siemens AG, Erlangen, Germany

<sup>3</sup>Cardiovascular MR Unit, Royal Brompton and Harefield NHS Foundation Trust, London, United Kingdom

\*Correspondence to: Davide Piccini, M.Sc., Pattern Recognition Lab, Department of Computer Science, Friedrich-Alexander University of Erlangen-Nuremberg, Martensstr 3, D-91058 Erlangen, Germany. E-mail: davide.piccini@informatik.uni-erlangen.de

Received 30 May 2011; revised 18 August 2011; accepted 13 September 2011. DOI 10.1002/mrm.23247

Published online 28 December 2011 in Wiley Online Library (wileyonlinelibrary.com).

3D radial acquisitions are usually performed using nonselective radio-frequency (RF) pulses such that the signal converging into the radial readouts is collected over the entire volume. In this scenario, fat saturation and  $T_2$  preparation (20,21) are sometimes insufficient to ensure the necessary contrast in the SI projections to isolate the signal of the blood pool. It has been shown that the presence of additional sources of bright signal, e.g., the spine, the chest wall, the arms, and the liver, can heavily perturb the results of a detection performed with center of mass (15). The use of more robust techniques, such as cross-correlation, is required to perform a reliable self-navigation. Therefore, all sources of additional bright signal must be suppressed such that the contribution of the blood pool in the SI projections can be reliably isolated.

In this work, a new technique for improved performance of self-navigated whole-heart coronary MRI has been developed, implemented, and tested. Data acquisition was performed with a 3D radial balanced Steady-State Free Precession (SSFP) sequence featuring a spiral phyllotaxis pattern (16), adapted to self-navigation (22). An innovative technique to suppress the additional bright signal from the arms and the chest wall is described, which allows to isolate the blood pool. This technique is based on the combination of the output signals from a phased-array surface receiver coil, placed on the chest. Furthermore, an algorithm for the automatic segmentation of the blood pool within the reference SI projections is proposed. Signal suppression, automatic segmentation, and motion detection and compensation were fully integrated in the data acquisition and reconstruction framework to allow a fast and easy workflow for coronary MR imaging. The results of the self-navigation were compared with the navigator-gated technique in 10 healthy volunteers.

## MATERIALS AND METHODS

### Isolation of the Blood Pool

In general, reliable isolation of the bright signal of the blood pool is essential to achieve robust self-navigation. In the case of nonselective 3D radial acquisitions, the input data used for self-navigation are degraded by several additional sources of bright signal: the anterior chest wall, the spine, the lateral chest wall, the arms, and the liver. It has been demonstrated that the signal from the anterior chest wall can be efficiently suppressed by a saturation slab (23). Furthermore, the signal originating from the spine can be significantly reduced by just excluding the signal from the posterior phased-array coil in postprocessing. In contrast, the suppression of the signal originating from the lateral structures, i.e., the arms and the lateral chest wall, is a more challenging task.

Similar to the methodology used for the spine, the exclusion of the lateral coil elements of the anterior phased-array coil was initially attempted to exclude the signal contribution of the lateral structures. However, a significant amount of lateral signal was still caught by the central coil elements. Therefore, a new targeted signal combination was considered to exploit advantageously the hardware structure of the anterior phased-array coil. In general, a mode matrix technology (Siemens AG, Healthcare Sector,

Erlangen, Germany) is implemented in the hardware of some of the phased-array coils of Siemens system (24). In particular, in the anterior phased-array coil, the signals from the right (R), middle (M), and left (L) coil elements are amplified and combined to form a set of three mode signals, referred to as primary mode (P), secondary mode (S), and tertiary mode (T). The P mode can be regarded as a one-channel circularly polarized (CP) coil, which is used for standard imaging. An example is shown, in magnitude  $|\mathcal{F}\mathcal{F}\mathcal{T}\{P\}|$ , in Fig. 1a.a1. Because of the contribution of the additional lateral signal, the bright signal of the blood pool is not clearly isolated from the background in the SI projections, Fig. 1a.b1. As it can be deduced from the signal  $|\mathcal{F}\mathcal{F}\mathcal{T}\{S\}|$ , displayed in Fig. 1b, the largest component that forms the S mode originates from the lateral coil elements, whereas the central portion is almost completely excluded. A combination C of the two modes, obtained by subtraction of  $|\mathcal{F}\mathcal{F}\mathcal{T}\{S\}|$  from  $|\mathcal{F}\mathcal{F}\mathcal{T}\{P\}|$ , efficiently suppresses the signal from the lateral structures, Fig. 1c.a1. Although the implementation of the channel combination uses the mode matrix hardware, this method can be generalized for other configurations of phased-array surface coils with right, left, and middle coil elements. The mathematical formulation of the signal suppression applied to the SI readouts is given in Eq. 1:

$$C_{SI} = |\mathcal{F}\mathcal{F}\mathcal{T}\{P_{SI}\}| - |\mathcal{F}\mathcal{F}\mathcal{T}\{S_{SI}\}|$$

$$= \left| \mathcal{F}\mathcal{F}\mathcal{T} \left\{ \frac{(R_{SI} - L_{SI})}{2} - j \frac{M_{SI}}{\sqrt{2}} \right\} \right| - \left| \mathcal{F}\mathcal{F}\mathcal{T} \left\{ \frac{(R_{SI} + L_{SI})}{\sqrt{2}} \right\} \right|, \quad [1]$$

where  $P_{SI}$  and  $S_{SI}$  represent the complex readouts with SI orientations obtained, respectively, from the primary and secondary modes, and  $R_{SI}$ ,  $L_{SI}$ , and  $M_{SI}$  are the complex SI readouts from the right, left, and middle coil elements. The symbol  $j$  represents the imaginary unit and the  $|\cdot|$  operator computes the absolute value of the signal pixelwise. Eventually  $\mathcal{F}\mathcal{F}\mathcal{T}\{X_{SI}\}$  represents the SI projection of the SI readout  $X_{SI}$ , whereas  $C_{SI}$  is the SI projection resulting from the channel combination. After the channel combination is performed, the additional bright signal is suppressed in the SI projections and the blood pool is reliably isolated, Fig. 1c.b1.

### Segmentation and Motion Compensation

A reliable identification of the structure corresponding to the blood pool is essential to compute its motion using cross-correlation. Although the channel combination provides the suppression of the additional bright lateral signal, this method does not ensure the blood pool to be the only, or at least the brightest, isolated structure within the SI projections. Hence, an algorithm was developed, which segments the blood pool in four automatic steps. This algorithm was applied, after intensity normalization, to the reference SI projection  $F$  that is obtained from the very first acquired readout.

The four steps are as follows: 1) The index of a local maximum within the blood pool,  $M$ , is found in an initial search range around the central point of the SI projection, equal to one-eighth of the total length of the projection.

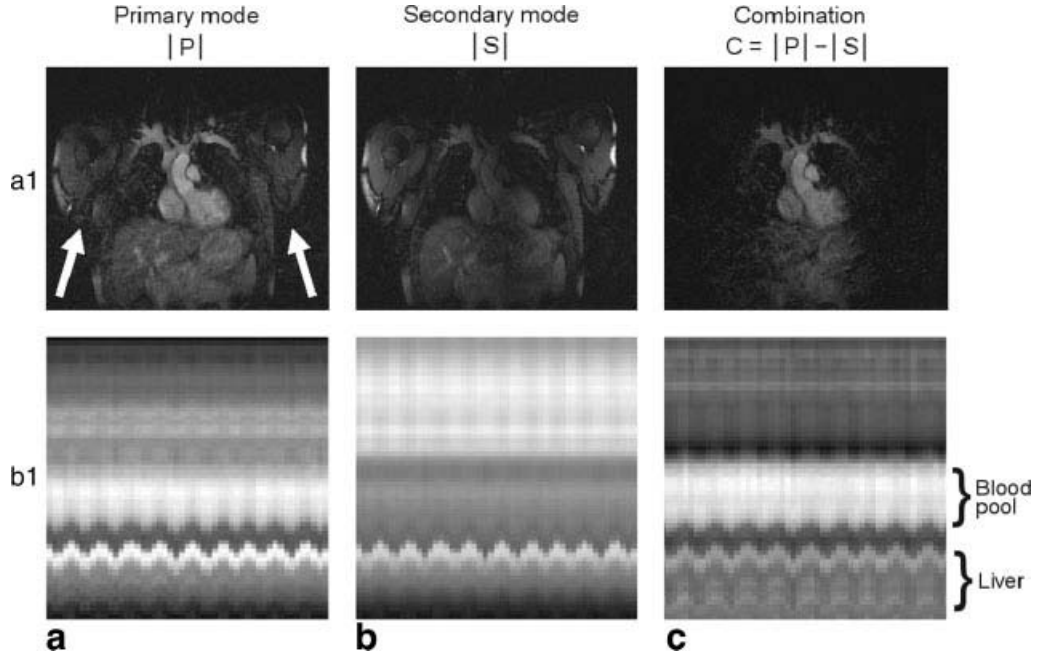


FIG. 1. Example of the suppression of the bright signal of the lateral structures by the combination of the mode signals from the anterior phased-array coil. While top row shows three two-dimensional coronal slices, obtained with standard Cartesian acquisitions from one of the volunteers, bottom row displays three series of SI projections acquired with the 3D radial trajectory, in the same volunteer, in 50 consecutive heartbeats. Column (a) displays the magnitude of the signal reconstructed with the primary mode: in this case the blood pool is not clearly isolated from the background in the series of SI projections (a.b1), due to the contribution of bright signal from the lateral structures (a.a1, white arrows). As the magnitude of the signal reconstructed with the secondary mode, displayed in (b), originates predominantly from the lateral coil elements, an advantageous combination of the two mode signals is implemented. If  $|\mathcal{FFT}\{S\}|$  is subtracted from  $|\mathcal{FFT}\{P\}|$ , then the bright signal of the lateral structures is efficiently suppressed (c.a1) and a reliable isolation of the bright signal of the blood pool in the SI projections is possible (c.b1).

A second point  $m$ , representing the index of the local minimum candidate, is iteratively moved outward, Fig. 2a. 2) At each iteration, two areas,  $A_1$  and  $A_2$ , are computed and compared.  $A_1$ , highlighted by diagonal stripes in Fig. 2b, is the area of the trapezoid delimited by the vertices  $F(M)$  and  $F(m)$  on the projection and by the indices  $M$  and  $m$  on the abscissa.  $A_2$  is area under the curve of the projection, spanned from index  $M$  to  $m$ . The stopping criterion is reached when the former exceeds the latter, Eq. 2.

$$A_1 = \frac{(F(M) + F(m)) \cdot |m - M|}{2} > \sum_{i=M}^m F(i) = A_2 \quad [2]$$

3)  $m$  is then assigned to the index corresponding to the local minimum within the current  $[M, m]$  interval, Fig. 2c. 4) Finally, the indices  $i_1$  and  $i_2$ , corresponding to  $F(i_k) \simeq 0.5 \cdot (F(M) - F(m))$ , where  $k = 1, 2$  and the symbol  $\simeq$  refers to the closest pixel, represent the final result of the segmentation, Fig. 2d. The segmented section  $[i_1, i_2]$  of the blood pool in the reference SI projection is then cross-correlated with all the successive normalized SI projections. This allows to compute the respiratory shift in SI direction, in pixels, corresponding to each interleave. Motion correction is performed in  $k$ -space, prior to the interpolation of the radial readouts onto the Cartesian grid, by multiplication with a linear phase, according to the Fourier shift theorem. The linear phase for each readout is computed according to the detected shift and to the polar angle between the current readout and the SI orientation (14).

## MR Experiments

The presented signal suppression method and the segmentation algorithm were fully integrated in the Siemens data acquisition and image reconstruction framework. The new method for self-navigation was compared with a navigator-gated approach featuring the same acquisition protocol. In vivo experiments were performed on 10 healthy volunteers—six males and four females, age:  $35 \pm 12.5$  years—after written consent was obtained. The imaging platform was a 1.5 T MAGNETOM Avanto scanner (Siemens AG, Healthcare Sector), with software release syngo MR B17A. A total of 12 elements of the anterior and posterior phased-array coils were activated for signal reception. Data acquisition was performed with a 3D radial trajectory implementing the spiral phyllotaxis pattern (16), adapted to self-navigation (22). All measurements were interleaved and ECG-triggered. A two-dimensional cine-scan with transversal slice orientation, prior to the whole-heart measurement, was used to precisely determine the individual delay of the acquisition window, needed to target the cardiac rest period in end diastole (3). The cubic field of view was positioned in such a way that the first readout of every interleave was oriented along the SI direction.  $T_2$ -prepared, fat-saturated, balanced SSFP imaging was performed for both navigator-gated and self-navigated acquisitions with the following parameters: pulse repetition time/echo time 3.0/1.52 ms, FOV (220 mm)<sup>3</sup>, matrix 192<sup>3</sup>, acquired voxel size (1.15 mm)<sup>3</sup>, flip angle 90°, and

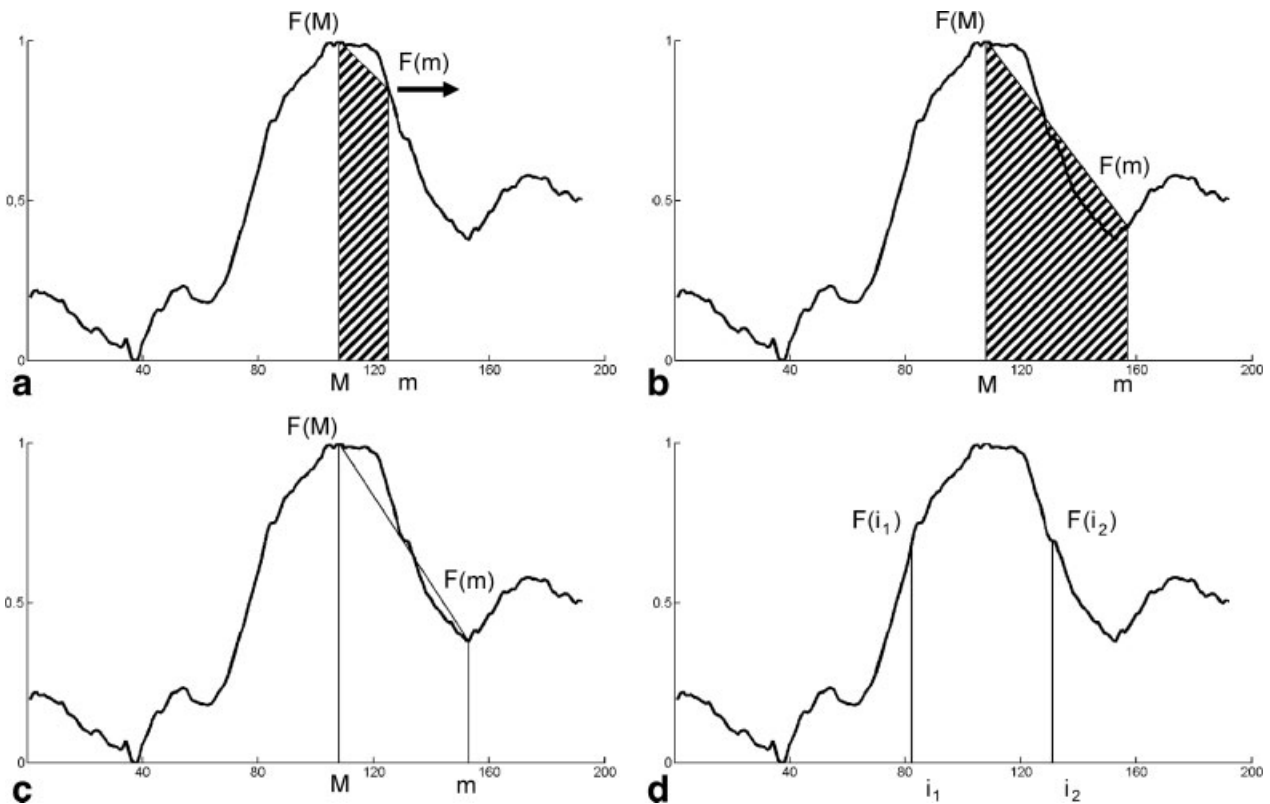


FIG. 2. Graphical representation of the four-steps algorithm for the automatic segmentation of the blood pool in the normalized reference SI projection,  $F$ . (a) The index of a local maximum  $M$  is detected within a neighborhood of the central point of the projection and a second index  $m$  is iteratively moved outward. (b) A criterion based on the area under the curve between  $M$  and  $m$  is used to stop the iterations. (c) The index corresponding to the local minimum between these two points is chosen as the final  $m$ . (d) Finally, two indices  $i_1$  and  $i_2$ , corresponding to the amplitude of 50% of the difference between  $F(M)$  and  $F(m)$  are selected as final result of the segmentation.

receiver bandwidth 898 Hz/Px. A total of 11,687 radial readouts were acquired in 377 heartbeats. This resulted in an overall undersampling ratio of 20%, with respect to the Nyquist limit. To automatically avoid foldover artifacts, 2-fold oversampling was applied in the readout direction. For gated acquisitions, a crossed-slice spin echo navigator was accurately positioned on the dome of the right hemidiaphragm. The width of the gating window of the navigator was 5 mm and slice tracking with a fixed correlation factor of 0.6 (25) was used. For self-navigated acquisitions, motion correction was applied to 100% of the acquired interleaves. A dummy interleave, without data acquisition, was applied before the beginning of the actual measurement to avoid artifacts from signal oscillations on the reference projection.

As a quality control during self-navigated acquisitions, all SI projections were visualized with the inline display (Siemens AG, Healthcare Sector). The quality control enabled the operator to assess the successful isolation of the blood pool for all projections, the correctness of the segmentation and the plausibility of the feedback of the cross-correlation. This procedure allowed an early reaction at the beginning of the acquisitions, in case the FOV was incorrectly positioned by the operator, such that a wrong structure was initially segmented. Furthermore, the feedback of the beam navigator was acquired as well during self-navigated acquisitions and used for data analysis.

## Data Analysis

Because of the absence of a ground truth on the actual respiratory motion of the heart, the analysis of the data was performed in two steps. First, a technical validation of the new method was accomplished and then the datasets acquired with the new method were compared with the navigator-gated acquisitions for acquisition time and image quality. As for the technical validation, the feedback provided by the cross-correlation on the SI projections was compared with the feedback on the position of the diaphragm, provided by the beam navigator, in all self-navigated acquisitions. To test the improvements obtained with the new technique, self-navigated motion detection was performed, for all volunteers, in three different configurations. The SI projections were cross-correlated using: 1) the P mode and the complete reference SI projection, 2) the signal combination and the complete reference SI projection, and 3) the proposed approach. For each configuration and for each volunteer, the feedback from the self-navigation and that from the navigator were plotted, for all interleaves, in a common graph to visually assess their synchronicity. A strong synchronicity was interpreted as the proof of principle that a motion correlated to the respiratory cycle was detected by the self-navigation (25). A quantification of the linear dependence between the two feedbacks was obtained by computing the Pearson

product-moment correlation coefficient (PMCC) (26) in Matlab 7.3 (The MathWorks Inc., Natick, MA). In addition, in case of strong visual synchronicity and high PMCC, the slope of the linear regression between the feedback of the self-navigation and of the cross-correlation was computed. The value of the slope was considered as an estimation of the subject-specific correlation factor, extended to the full respiratory cycle.

The total acquisition time of the self-navigated method was compared with the total acquisition time of the navigator-gated technique to estimate the average improvement in scan efficiency. The 3D isotropic image data, acquired with both methods, were reformatted in post-processing with CoronaViz (Work in Progress software, Siemens Corporate Research, Princeton, NJ) to visualize the right coronary artery (RCA), the left anterior descending artery (LAD), and the left coronary circumflex (LCX). The results of the off-line reformat were used for qualitative assessment of the image quality and to compare the number of detectable coronary arteries with the two acquisition schemes. A coronary artery that could be manually segmented for a length of at least 40 mm was defined as detectable. Vessel length was assessed for all the RCAs, LADs, and LCXs that could be detected in both groups of datasets. Finally, the inverse of the average distance between 20 and 80% of the signal intensity profiles on both sides of a cross-sectional line, perpendicular to the axes of the coronary vessel, was used for the calculation of the vessel sharpness as described in Ref. (27). The final value of the vessel sharpness for each single coronary was averaged on eight manually selected cross-sections, distributed along the whole length of the segmented vessel. Statistical comparisons on all the results obtained on the navigator-gated and the self-navigated acquisitions were performed by means of a paired two-tailed Student's *t*-test. *P* values of 0.05 or less were considered as statistically significant.

## RESULTS

Navigator-gated as well as self-navigated whole-heart coronary MRI acquisitions were successful in all volunteers. The visual assessment of the motion detection when the cross-correlation was applied to the complete SI projection in P mode showed that almost no motion could be detected in three volunteers. In this case, the synchronicity with the feedback from the beam navigator was low in all volunteers and the total average value of the PMCC was only  $0.67 \pm 0.54$ . After the proposed signal combination, the blood pool was visualized as an isolated structure in all SI projections. When cross-correlation was applied to the complete projection after signal combination, the visualized synchronicity showed a clear improvement. The average PMCC increased to  $0.81 \pm 0.08$ . Nevertheless, the value of the slope of the linear regression was lower than 0.2 for five volunteers and the total average was only  $0.32 \pm 0.24$ . The proposed algorithm for automatic segmentation, performed after signal combination, was always successful, despite the high variability of the shape of the SI profiles among different subjects. An example of the feedback from the motion detection obtained with the new method is displayed, with two red lines, in Fig. 3a over a series of SI projections acquired in 50 consecutive heartbeats. In

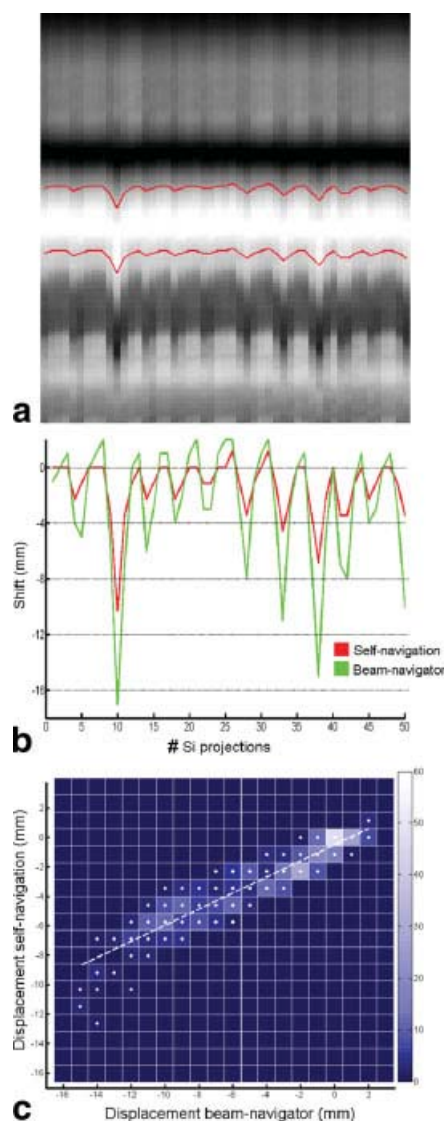


FIG. 3. The respiratory motion detected by cross-correlation on the bright signal of the blood pool was compared for validation with the position of the diaphragm, detected by the beam navigator. Because of the intrinsic limitations of the navigator-gated methods, the comparison with the position of the diaphragm is considered as a proof of principle for the proposed motion detection and not as a ground truth on the real respiratory motion of the heart. A series of 50 SI projections, acquired in 50 consecutive heartbeats, in one of the volunteers, is displayed in (a). The bright region in the central part of the projections is the isolated signal originating from the blood pool. The two red lines visualize the respiratory displacement, detected with the cross-correlation algorithm, of the two indices ( $i_{1,2}$ ) selected by the segmentation algorithm. The results of the cross-correlation are overlapped to the corresponding results of the beam-navigator (green line) in (b). It appears to be evident that the motion detected with the two methods is synchronous. A plot showing the displacements measured with the self-navigation versus the corresponding displacements detected by the beam-navigator is shown in (c). The number of occurrences of all pairs of values, represented by the white dots, is color coded in the background and the linear regression is represented by the white line. The precision of the self-navigation is given by the acquired voxel size, 1.15 mm, whereas that of the beam navigator was 1.0 mm. For this specific volunteer, the value of the PMCC was 0.94 and that of the slope of the linear regression was 0.54.

Table 1

Numerical results and statistical significance of the comparison between the self-navigated acquisitions and the reference navigator-gated acquisitions. The acquisition time was more than halved with comparable results as for vessel sharpness and length

	Reference vessel	Navigator-gated approach	Self-navigated approach	Significance of difference <sup>a</sup>
Detected/total	RCA	10/10	10/10	
	LAD	9/10	10/10	
	LCX	8/10	8/10	
Vessel length (mm)	RCA	101.65 ± 23.72	113.46 ± 19.03	N.S.
	LAD	91.84 ± 39.46	99.52 ± 31.60	N.S.
	LCX	68.21 ± 12.88	71.62 ± 9.73	N.S.
Vessel sharp.	RCA	1.00 ± 0.23	1.09 ± 0.22	<i>P</i> < 0.05.
	LAD	1.03 ± 0.19	1.10 ± 0.24	N.S.
	LCX	1.16 ± 0.28	1.18 ± 0.22	N.S.
Scan time (min)		16.23 ± 6.28	6.07 ± 0.57	<i>P</i> < 0.01.
Scan efficiency (%)		41.16 ± 11.75	100 ± 0.0	<i>P</i> < 0.01.

<sup>a</sup> N.S. = not significant (Student's *t*-test)

addition, an example of the high synchronicity with the feedback from the beam navigator can be assessed in Fig. 3b, where the motion of the diaphragm is depicted by a green line. In this case, the average value of the PMCC was the highest,  $0.85 \pm 0.12$ , and confirmed the consistency of the motion estimation. With the new method, the average value of the slope of the linear regression between the result of the cross-correlation and the detection of the beam navigator, over all in vivo datasets, was  $0.47 \pm 0.30$ . This is graphically supported by Fig. 3b, where the curve of the self-navigation appears dampened if compared with the navigator. Figure 3c shows the displacement detected with the new self-navigation plotted against the SI shift of the right hemidiaphragm, detected with the navigator. The range of 1D, corrections varied, in average, between a minimum displacement of the blood pool of  $\pm 1.15$  mm, i.e., one pixel, and a maximum of  $\pm 12.6$  mm. Occasional “outliers”, with absolute values between 20 and 25 mm, were detected and corrected for three of the volunteers.

As reported in Table 1, with the full efficiency of the self-navigated method, the total acquisition time was reduced by more than 60%, compared with the navigator-gated reference. All RCAs could be segmented in both cases, whereas the segmentation of the LAD was possible in 9 of the 10 datasets acquired with navigator gating and in all 10 self-navigated acquisitions. The LCX could be segmented only in 8 datasets, the same for both acquisitions. The quantitative assessment of vessel length and sharpness, displayed in Table 1, shows a slight average superiority of the new method. Although the mean improvement in the detected vessel length and sharpness was, respectively, 8.3 and 5.8%, only the improvement in the vessel sharpness of the RCA showed a statistical significance ( $P < 0.05$ ). In comparison with the reference (Fig. 4a, c, and e), the image quality obtained with the self-navigation technique (Fig. 4b, d, and f) was equivalent or slightly superior in almost all cases. In only one case, although the distal part of the LAD was well visualized in the navigator-gated dataset (Fig. 5a), the corresponding part appeared blurred by the effect of the residual motion artifacts in the self-navigated dataset (Fig. 5b). In general, the presence of minor artifacts, due to uncompensated residual motion, could be noticed in all datasets.

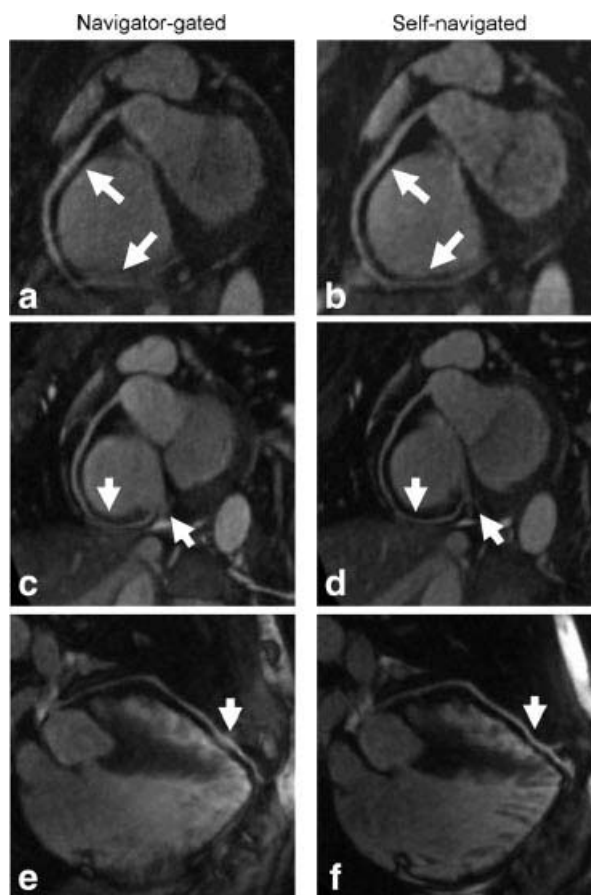


FIG. 4. Reformatted images of the RCA (a–d) and of the LAD (e–f) are depicted for reference acquisitions obtained with the navigator-gated technique (a, c, e) and with the new self-navigation (b, d, f). In the specific case of (a), the low scan efficiency of the navigator-gated technique resulted in poor image quality. The white arrows in (a) and (b) highlight the proximal and the distal part of the RCA: the dataset acquired with self-navigation displays superior vessel sharpness and length. The white arrows in (c, d) and (b, f) highlight regions where the new method resulted in an improved delineation of the coronary vessels, in two cases where similar image quality was obtained with both approaches. However, minor blurring artifacts due to uncompensated residual motion can still be noticed.

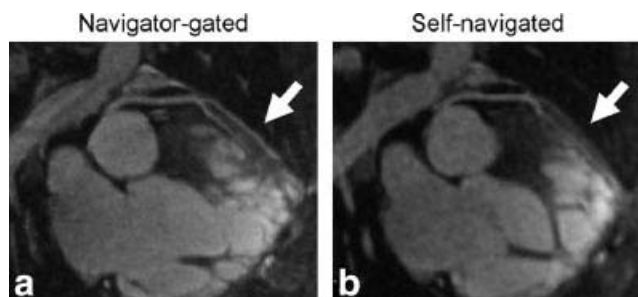


FIG. 5. Reformatted images of the LAD of one of the examined subjects are depicted for the acquisition performed with navigator-gated approach (a) in comparison with the new self-navigated approach (b). For the specific subject, the total acquisition time of the navigator-gated dataset was as low as 14.8 min. Although the distal part of the coronary vessel is well outlined in (a), the correspondent section is blurred in (b). In this case, the approximation of the respiratory motion to an SI translation was inadequate to achieve a good image quality with self-navigation and residual blurring artifacts are clearly visible (white arrows). The extension of the proposed algorithm for motion correction to more complex motion models can potentially overcome this limitation in self-navigated acquisitions.

## DISCUSSION

The static bright signal from the lateral structures affects the result of the cross-correlation, such that the respiratory motion of the heart can not be adequately detected. This is confirmed by the visual assessment of the insufficient or even null motion detection in some of the volunteers and, in general, by the low values of the PMCC. The proposed method for the isolation of the blood pool shows to perform robustly in a number of subjects and can be integrated in many of the modern MR systems. In case anterior phased-array coils with smaller coil elements are used, similar results might be obtained by the simple selection of the central elements. However, as this method is introduced to address the specific problem of the suppression of the lateral bright signal in the SI projections, its adaptation to different applications, such as dark blood acquisitions, might not be straightforward. An alternative approach could be slab-selective excitation. In this case, nevertheless, monitoring of the required specific absorption rate (SAR) and extension of the TR have to be considered. An alternative solution might be also found in the field of parallel RF transmission (28), which would allow spatially selective RF excitation.

The proposed automatic segmentation of the blood pool shows to improve the results obtained with the use of the complete SI projections after suppression of the lateral signal. In the latter case, in fact, even if the good synchronicity and the high PMCC indicate that, in principle, the respiratory motion is detected, the low values of the slope of the linear regression imply that the result of the cross-correlation is still biased by the presence of static structures within the projections (e.g., static bright signal on top of Fig. 3a). The proposed segmentation algorithm performs reliably as long as the FOV is placed correctly, i.e., if the blood pool is in the center. In this context, the radial 3D acquisition, with oversampling along each readout, highly simplifies the planning procedure. In the case of an inadequately placed FOV, the quality control allows a prompt

correction of the placement in an early stage of the acquisition, such that the temporal efficiency of the measurement is not affected. This control proved to be useful in particular with female volunteers, as the bright signal from the chest wall is not always completely suppressed by the anterior saturation slab. Moreover, the initial search range for the local maximum in the segmentation algorithm could be adapted for each acquisition to better fit the anatomy of each subject.

The superiority of the new self-navigated approach is confirmed by the strong visual synchronicity with the detection of the navigator and by the highest values of the PMCC. Figure 3c shows that the linear relationship between the displacement of the heart and the diaphragm is not constant over all the respiratory cycle and is stronger close to end-expiration, where most of the samples are located, in agreement with the literature (25). The average value of the slope of the linear regression is very similar to that which is recently reported in Ref. (29). The relatively high standard deviation of this value confirms that the correlation factor between the motion of the blood pool and the diaphragm is highly subject-dependent (11). The flat tops that can be observed in Fig. 3b originate from the fact that the precision of the cross-correlation, in the present implementation, is dictated by the actual image resolution. As self-navigation allows to estimate the respiratory motion directly on the imaged organ, motion correction can be extended from a narrow gating window of the navigator to the full respiratory cycle. As a consequence, all interleaves of the self-navigated approach feed into image reconstruction. Hence, with the new method, the total acquisition time depends only on the average heart-rate of the examined subject, and 100% success rate as well as 100% scan time efficiency are achieved. Moreover, the total duration of the measurement can be always estimated in advance. This feature makes the self-navigated method superior to navigator-gating both with respect to the planning of the single coronary MRI acquisition and for the integration of this technique into a complete cardiac examination.

The new method not only features major improvements in the detection of the coronaries in cases where navigator gating is affected by very low scan efficiency (Fig. 4a and b) but also results in a slightly improved sharpness of the coronary vessels in cases where similar image quality is obtained with both acquisitions (Fig. 4c–f). As the acquisition protocol was the same for both methods, the average slight improvement in image quality obtained with the self-navigation is considered to be mainly related to the reduced total acquisition time. In addition, the use of cross-correlation directly applied to the segmented blood pool makes the 1D motion correction performed with the new approach more reliable than with the navigated acquisitions, where the motion is estimated indirectly, on the diaphragm. Nevertheless, artifacts caused by uncompensated residual motion and nonlinearities in self-navigated datasets suggest that the approximation of the respiratory motion to an SI translation is not always adequate (5,25). In particular, Fig. 5 provides an example where a better result was achieved with the navigator-gating technique. This can be explained by the fact that, as the acquisition is performed consistently within the same respiratory phase, all motion components are intrinsically

minimized in a navigator-gated setup. A similar effect could be obtained in self-navigation by selecting the reference SI projection “a posteriori” in an interleaved acquired during end-expiration. This would allow to maximize the number of interleaves acquired during the reference respiratory position and, thus, to minimize the number of 1D corrections. A subpixel precision of the 1D motion detection would be possible with the use of interpolation on the SI projections. Nevertheless, for a real improvement of the self-navigated method, the extension of the motion correction to more complex motion models needs to be explored first. An extended projection-based approach that makes use of the 3D positional information contained in all projections of the 3D radial trajectory is one possibility (30). Affine motion correction (31,32), furthermore, can be achieved with techniques based on image registration (33). A first attempt to implement a hybrid solution that combines self-navigation with image registration was recently proposed in Ref. (34).

Beyond these extensions, the possibility to perform coronary MRI at 3T would allow to obtain higher signal-to-noise ratio (SNR) and, therefore, an improved spatial resolution (35,36). If issues regarding the effectiveness of the  $T_2$  preparation (37), fat saturation, and off-resonance artifacts (38) are efficiently addressed at 3T, the presented method can be straightforwardly applied also to this setup. Furthermore, acceleration of the acquisition process could be obtained using reconstruction methods that exploit the redundancy of the information contained in the image and which can be integrated into the current implementation. As the signal combination based on the coil elements is used only for self-navigation, parallel imaging performances remain unaffected. In addition, the use of iterative reconstruction methods, such as compressed sensing (39), applied to radial 3D (40), might be considered. If the acquisition time is highly reduced, a more comfortable examination for the patient can be provided and the probability of involuntary motion of the examined subject is reduced. Eventually, if a high acceleration of the acquisition is achieved, applications of the current method in dynamic studies, e.g., whole-heart cine or perfusion MRI, might be considered.

## CONCLUSIONS

The described method for self-navigation, implementing automatic isolation and segmentation of the blood pool achieves a high reliability. This technique outperforms the existing navigator-gated approaches for simplicity of the examination setup, efficiency, and total scan time. With the new implementation, not only whole-heart coronary MRI can be performed without the use of a respiratory beam-navigator, but also the robustness and the success rate of the acquisition are highly improved by the use of cross-correlation. Furthermore, comparable or slightly superior results in image quality with respect to the current navigator-gated techniques are obtained. For these reasons, the described self-navigated approach is already appealing for extensive clinical studies. Finally, such an approach offers a sound basis for a future extension of the motion correction to models of higher complexity.

## REFERENCES

- Hauser TH, Manning WJ. The promise of whole-heart coronary MRI. *Curr Cardiol Rep* 2008;10:46–50.
- Stuber M, Weiss RG. Coronary magnetic resonance angiography. *J Magn Reson Imaging* 2007;26:219–234.
- Kim WY, Stuber M, Kissinger KV, Manning WJ, Andersen NT, Botnar RM. Impact of bulk cardiac motion on right coronary MR angiography and vessel wall imaging. *J Magn Reson Imaging* 2001;14:383–390.
- Ehman RL, Felmlee JP. Adaptive technique for high-definition MR imaging of moving structures. *Radiology* 1989;173:255–263.
- McLeish K, Hill LGD, Atkinson D, Blackall JM, Razavi R. A study of the motion and deformation of the heart due to respiration. *IEEE Trans Med Imaging* 2002;21:1142–1150.
- Danias PG, McConnell MV, Khasgiwala VC, Chuang ML, Edelman RR, Manning WJ. Prospective navigator correction of image position for coronary MR angiography. *Radiology* 1997;203:733–736.
- Deshpande VS, Krishnam MS, Ruehm SG, Finn JP, Laub GA. Non-contrast MR angiography of the heart and great vessels using SSFP with non-selective excitation. In: *Proceedings of the 14th Annual Meeting of ISMRM, Seattle, WA, USA; 2006.* p 383.
- Nguyen TD, Spincemaille P, Cham MD, Weinsaft JW, Prince MR, Wang Y. Free-breathing 3-dimensional steady-state free precession coronary magnetic resonance angiography: comparison of four navigator gating techniques. *Magn Reson Imaging* 2009;27:807–814.
- Jhooti P, Keegan J, Firmin DN. A fully automatic and highly efficient navigator gating technique for high-resolution free-breathing acquisitions: continuously adaptive windowing strategy. *Magn Reson Med* 2010;64:1015–1026.
- Stuber M, Botnar RM, Danias PG, Kissinger KV, Manning WJ. Sub-millimeter three-dimensional coronary MR angiography with real-time navigator correction: comparison of navigator locations. *Radiology* 1999;212:579–587.
- Taylor AM, Jhooti P, Firmin DN, Pennell DJ. Automated monitoring of diaphragm end-expiratory position for real-time navigator echo MR coronary angiography. *J Magn Reson Imaging* 1999;9:395–401.
- Nehrke K, Bornert P, Manke D, Bock JC. Free-breathing cardiac MR imaging: study of implications of respiratory motion—initial results. *Radiology* 1999;220:810–815.
- Spuentrup E, Manning WJ, Botnar RM, Kissinger KV, Stuber M. Impact of navigator timing on free-breathing submillimeter 3D coronary magnetic resonance angiography. *Magn Reson Med* 2002;47:196–201.
- Stehning C, Börner P, Nehrke K, Eggers H, Stuber M. Free-breathing whole-heart coronary MRA with 3D radial SSFP and self-navigated image reconstruction. *Magn Reson Med* 2005;54:476–480.
- Lai P, Larson AC, Bi X, Jerecic R, Li D. A dual-projection respiratory self-gating technique for whole heart coronary MRA. *J Magn Reson Imaging* 2008;28:612–620.
- Piccini D, Littmann A, Nelles-Vallespin S, Zenge MO. Spiral phyllotaxis: the natural way to construct a 3D radial trajectory in MRI. *Magn Reson Med* 2011;66:1049–1056.
- Stehning C, Börner P, Nehrke K, Eggers H, Dössel O. Fast isotropic volumetric coronary MR angiography using free-breathing 3D radial balanced FFE acquisition. *Magn Reson Med* 2004;52:197–203.
- Lauzon ML, Rutt BK. Effects of polar sampling in  $k$ -space. *Magn Reson Med* 1996;36:940–949.
- Barger AV, Block VF, Toropov Y, Grist TM, Mistretta CA. Time-resolved contrast-enhanced imaging with isotropic resolution and broad coverage using an undersampled 3D projection trajectory. *Magn Reson Med* 2002;48:297–305.
- Wright GA, Nishimura DG, Macovski A. Flow-independent magnetic resonance projection angiography. *Magn Reson Med* 1991;17:126–140.
- Brittain JH, Hu BS, Wright GA, Meyer CH, Macovski A, Nishimura DG. Coronary angiography with magnetization-prepared T2 contrast. *Magn Reson Med* 1995;33:689–696.
- Piccini D, Littmann A, Nelles-Vallespin S, Zenge MO. Robust and fully integrated one dimensional respiratory self-navigation for whole-heart coronary MRI. In: *Proceedings of the 19th Annual Meeting of ISMRM, Montreal, Canada; 2011.* p 1259.
- Stuber M, Botnar RM, Danias PG, Sodickson DK, Kissinger KV, Van Cauteren M, De Becker J, Manning WJ. Double-oblique free-breathing high resolution three-dimensional coronary magnetic resonance angiography. *J Am Coll Cardiol* 1999;34:524–531.
- Reykowski A, Blasche M. Mode matrix—a generalized signal combiner for parallel imaging arrays. In: *Proceedings of the 12th Annual Meeting of ISMRM, Kyoto, Japan; 2004.* p 1587.

25. Wang Y, Riederer SJ, Ehman RL. Respiratory motion of the heart: kinematics and the implications for the spatial resolution in coronary imaging. *Magn Reson Med* 1995;33:713–719.
26. Rodgers JL, Nicewander WA. Thirteen ways to look at the correlation coefficient. *Am Stat* 1988;42:59–66.
27. Li D, Carr JC, Shea SM, Zheng J, Deshpande VS, Wielopolski PA, Finn JP. Coronary arteries: magnetization-prepared contrast-enhanced three-dimensional volume-targeted breath-hold MR angiography. *Radiology* 2001;219:270–277.
28. Katscher U, Börnert P. Parallel RF transmission in MRI. *NMR Biomed* 2006;19:393–400.
29. Jahnke C, Nehrke K, Paetsch I, Schnackenburg B, Gebker R, Fleck E, Nagel E. Improved bulk myocardial motion suppression for navigator-gated coronary magnetic resonance imaging. *J Magn Reson Imaging* 2007;26:780–786.
30. Wieben O, Barger AV, Block WF, Mistretta CA. Correcting for translational motion in 3D projection reconstruction. In: *Proceedings of the 9th Annual Meeting of ISMRM, Glasgow, Scotland; 2001.* p 737.
31. Manke D, Nehrke K, Börnert P, Rösch P, Dössel O. Respiratory motion in coronary magnetic resonance angiography: a comparison of different motion models. *J Magn Reson Imaging* 2002;15:661–671.
32. Manke D, Nehrke K, Börnert P. Novel prospective respiratory motion correction approach for free-breathing coronary MR angiography using a patient-adapted affine motion model. *Magn Reson Med* 2003;50:122–131.
33. Bhat H, Ge L, NIELLES-VALLESPIN S, ZUEHLSORFF S, LI D. 3D radial sampling and 3D affine transform-based respiratory motion correction technique for free-breathing whole-heart coronary MRA with 100% scan efficiency. *Magn Reson Med* 2011;65:1269–1277.
34. Piccini D, Littmann A, Xue H, Guehring J, Zenge MO. The next step in self-navigated coronary MRI: a hybrid approach for affine motion correction. In: *Proceedings of the 19th Annual Meeting of ISMRM, Montreal, Canada; 2011.* p 1271.
35. Bi X, Deshpande V, Simonetti O, Laub G, Li D. Three-dimensional breathhold SSFP coronary MRA: a comparison between 1.5 T and 3.0 T. *J Magn Reson Imaging* 2005;22:206–212.
36. Xie J, Lai P, Bhat H, Li D. Whole-heart coronary magnetic resonance angiography at 3.0 T using short-TR steady-state free precession, vastly undersampled isotropic projection reconstruction. *J Magn Reson Imaging* 2010;31:1230–1235.
37. Nezafat R, Ouwerkerk R, Derbyshire AJ, Stuber M, McVeigh ER. Spectrally selective B1-insensitive T2 magnetization preparation sequence. *Magn Reson Med* 2009;61:1326–1335.
38. Shah S, Kellmann P, Greiser A, Weale PJ, Zuehlsdorff S, Jerecic R. Rapid fieldmap estimation for cardiac shimming. In: *Proceedings of the 17th Annual Meeting of ISMRM, Honolulu, Hawaii, USA; 2009.* p 566.
39. Lustig M, Donoho D, Pauly JM. Sparse MRI: the application of compressed sensing for rapid MRI imaging. *Magn Reson Med* 2007;58:1182–1195.
40. Doneva M, Eggers H, Rahmer J, Börnert P, Mertins A. Highly undersampled 3D golden ratio radial imaging with iterative reconstruction. In: *Proceedings of the 16th Annual Meeting of ISMRM, Toronto, Canada; 2008.* p 336.